SHEAR BANDING IN WORMLIKE MICELLAR SOLUTIONS

Summer School on Neutron Scattering and Reflectometry
NG3 SANS Team
NIST Center for Neutron Research
May 10-14, 2010

ABSTRACT

Wormlike micelles are an important class of surfactant micellar architectures that find use in applications ranging from consumer products to energy and nanomaterials. Many wormlike micellar systems exhibit a flow instability known as shear banding, characterized by an inhomogeneous flow field. Although many of the proposed mechanisms and theories for shear banding revolve around fluid microstructure, very little has been done to confirm them using direct microstructural measurements. Flow-small angle neutron scattering (flow-SANS) techniques are emerging as a powerful tool to interrogate the structure of wormlike micelles and other complex fluids under flow, enabling rigorous testing of theories and development of structure property relationships for shear banding. This experiment will utilize the full compliment of flow-SANS methods currently available to determine the underlying microstructural basis for shear banding in a model wormlike micellar fluid.

1. INTRODUCTION

1.1. Wormlike micelles

Surfactants are molecules comprised of two (or more) different chemical moeties that, when dissolved in a solvent, display different solvophilic and solvophobic properties. Most surfactants consist of a water-soluble, hydrophilic head group, and a water-insoluble hydrophobic tail, typically a hydrocarbon. An illustration of such a molecule is shown in Figure 1, where the head group is depicted as a sphere with some effective volume covalently bound to a hydrocarbon chain. For sufficiently dilute conditions, the surfactant will exist as monomers in aqueous solution, where the head group will be solvated by water. Due to the large entropic penalty from exposure of the hydrocarbon chain to the solvent, the surfactant will spontaneously aggregate above a concentration referred to as the critical micelle concentration (CMC). This aggregation results in the formation of micelles with a hydrophobic interior containing the hydrocarbon tails, which is separated from the solvent by the hydrophilic head groups.

Above the CMC, most surfactants form a single, isotropic phase over a large range of thermodynamic conditions, referred to as the L_1 phase. A variety of micelle morphologies are observed in the L_1 phase, including globules, rods, wormlike micelles, and branched micellar networks. This work is primarily concerned with wormlike micelles (WLMs), which are long, flexible threadlike surfactant aggregates. In a solution of sufficient concentration, WLMs will entangle to form a viscoelastic network, much like an entangled polymer solution. An example of an entangled WLM fluid is shown Figure 2. These viscoelastic WLMs exhibit a hierarchy of length scales and associated dynamics, all of which affect the resulting fluid properties and all of

which can be readily tuned through a number of different means, including temperature, pressure, and various chemical additives.

Because of this ability, in combination with their detergency and structure, WLMs have become ubiquitous to a wide variety of industrial processes and consumer products. Most readers will be familiar with traditional applications in the latter, where wormlike micelle-forming surfactants are a primary component and/or active agent in body washes, shampoos, household cleaners, and cosmetics. More recent applications of have been in oilfield completion, stimulation, and production. Finally, WLMs have been used in the rapidly emerging field of nanotechnology as templates for organic and inorganic nanoparticles and colloical arrays.

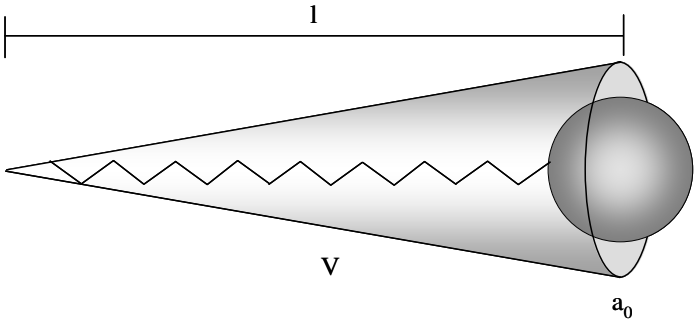

Figure 1. Illustration of a typical surfactant molecule including head group with projected area a_0 and tail group with volume V and length l.

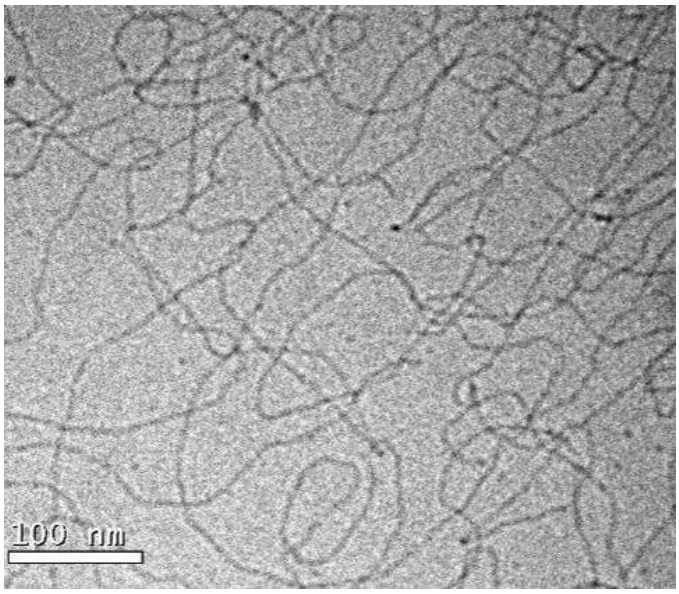

Figure 2. An entangled wormlike micellar solution imaged by cryogenic transmission electron microscopy. (Image taken by T.K. Hodgdon)

This work deals with ionic surfactant, where the head group comprises a salt moiety. A prototypical phase diagram of ionic surfactants is shown in Figure 3, plotted in a space of temperature, T, and surfactant volume fraction, ϕ. Below the CMC, surfactants exist only as monomers in solution. Above the CMC, globular micelles are spontaneously formed. A decrease in temperature in the L_1 phase will result in a sphere-to-rod transition and resulting growth of WLMs under relatively dilute surfactant concentrations. As the concentration of surfactant is increased, both the contour length and number of micelles increase simultaneously, resulting in rapid changes in mesoscale structure of the fluid, similar to what is observed in polymer solutions of increasing molecular weight or concentration.

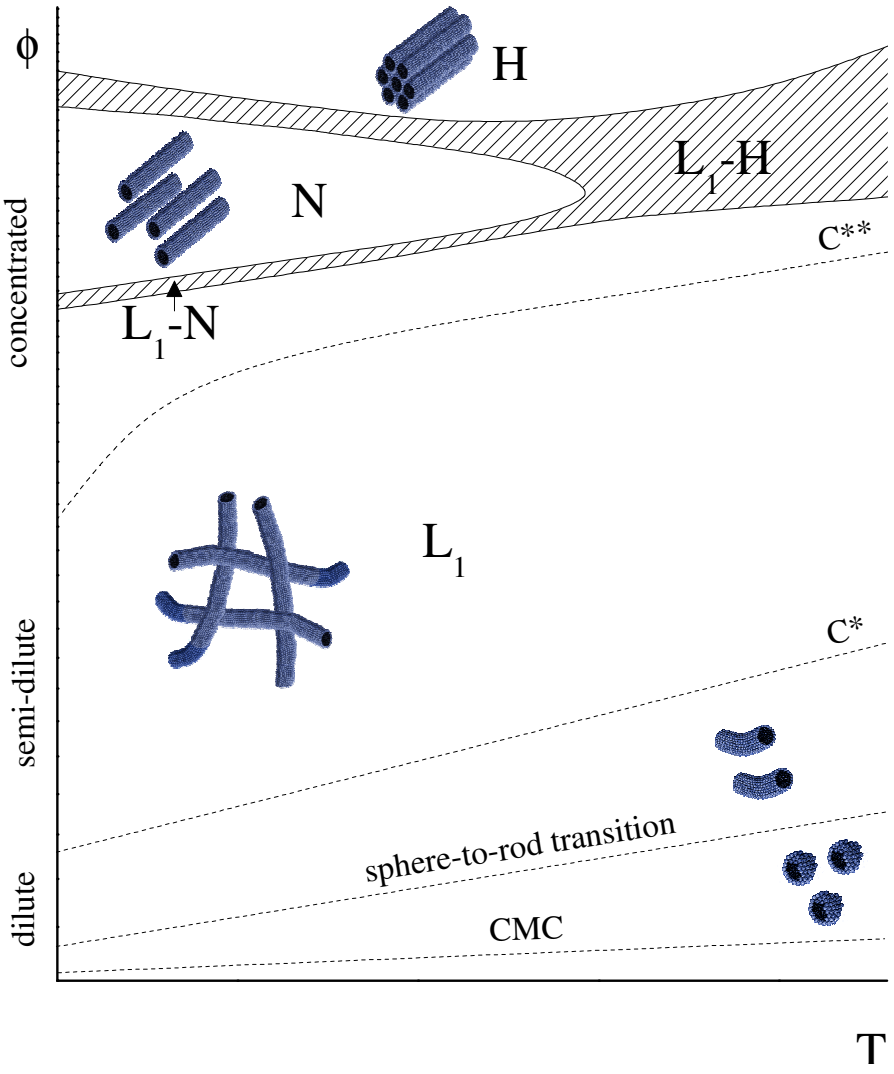

Figure 3. Prototypical phase diagram for ionic surfactants in the micellar phase (L_1) showing the critical micelle concentration (CMC), sphere-to-rod transition, overlap concentration (c*), and Onsager regime (c**), as well as the liquid crystalline nematic (N) and hexagonal (H) phases.

At sufficiently high concentration, micellar chains will transition from dilute to semi-dilute conditions at a critical concentration referred to as the overlap concentration, c^*, defined in a manner similar to that for polymer solutions. As the concentration of micelles is increased even further, the micelles will form an entangled network due to an increasing degree of overlap between micellar chains. The mesoscale structure of an entangled micellar network is depicted in Figure 4, and has characteristic length scales such as the overall contour length (L_c), length between entanglements (l_e), and mesh size (ξ_m) associated with the entangled network. It is this entanglement that gives rise to viscoelasticity in WLMs. Because increases in surfactant concentration can result in increases in both the number and length of micelles, the viscosity and viscoelasticity of WLMs can increase quite rapidly as compared to polymer solutions. This effect is further exaggerated for ionic micelles due to electrostatic repulsions between like-charged micelles.

As the number of micelles in solution is increased above the entanglement concentration, the number of entanglements will increase, resulting in a decrease in l_e. Once l_e is decreased to the point where $l_e \sim l_p$, where l_p is the persistence length above which the micelles are flexible, the micelles can be phenomenologically described by a suspension of infinitely long, rigid rods at a critical concentration of c^*. This limit is typically referred to as the Onsager regime, so-named for the author of seminal theoretical descriptions of concentrated rigid rod suspensions. In the Onsager regime, the packing of micelles in solution results in the formation of liquid crystalline phases. At sufficient packing of micelles, this will result in an isotropic-nematic (I-N) transition. The nematic (N) phase results from a gain in local entropy at the expense of global orientation due to excluded volume interactions between micelles, where the micelles preferentially align along one direction. Further packing of micelles results in a transition to a hexagonal (H) phase, where micelles adopt both orientational and translational order as they approach the close-packed limit.

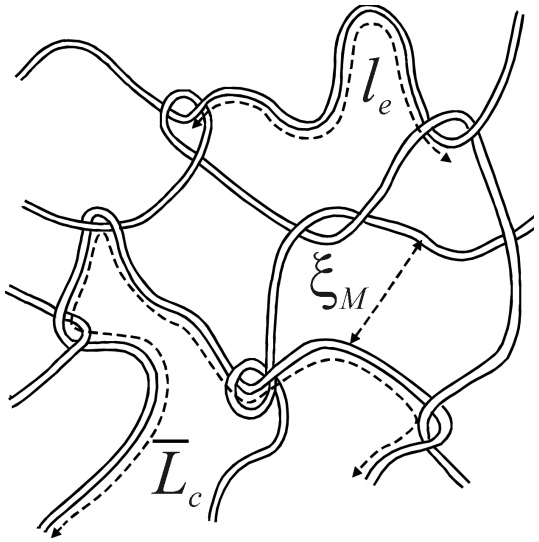

Figure 4. Illustration of an entangled micellar network and associated length scales.

To this point, the phase behavior of ionic surfactant has been discussed exclusively at thermodynamic equilibrium. However, non-equilibrium applied fields, such as shear flow, are known to directly affect the phase behavior of WLMs. Many surfactant systems exhibit a specific flow instability known as shear banding, resulting in non-homogenous flow of the fluid. In many cases, shear banding is thought to arise from shear-induced phase transitions in the L_1 phase. Despite a large body of experimental work on these so-called shear banding WLMs, relatively little is known experimentally regarding how these flow instabilities relate directly to the underlying equilibrium surfactant phase behavior and microstructure.

1.1. Shear banding

Shear banding in wormlike micelles was first studied, though unknowingly, in aqueous solutions of the cationic surfactants in the presence of hydrotropic salts. In these experiments, a so-called "stress plateau" in strain-controlled rheological measurements (Figure 5a), where the apparent steady state shear stress was nearly constant over several decades in applied shear rate. It was hypothesized that this extreme case of shear thinning was a result of an inhomogeneous flow within the material. This hypothesis was later reinforced by polarized light visualization, which showed the distinct formation of two fluid "bands" in Taylor Couette flow, of relatively high and low birefringence with a seemingly sharp interface, formed along the flow gradient direction. These birefringence bands have been shown by examining the associated velocity profiles to indeed correspond with separation of the flow field into two fluid layers, one at a high local shear rate, the high-shear band and one at a low local shear rate, the low-shear band (Figure 5b).

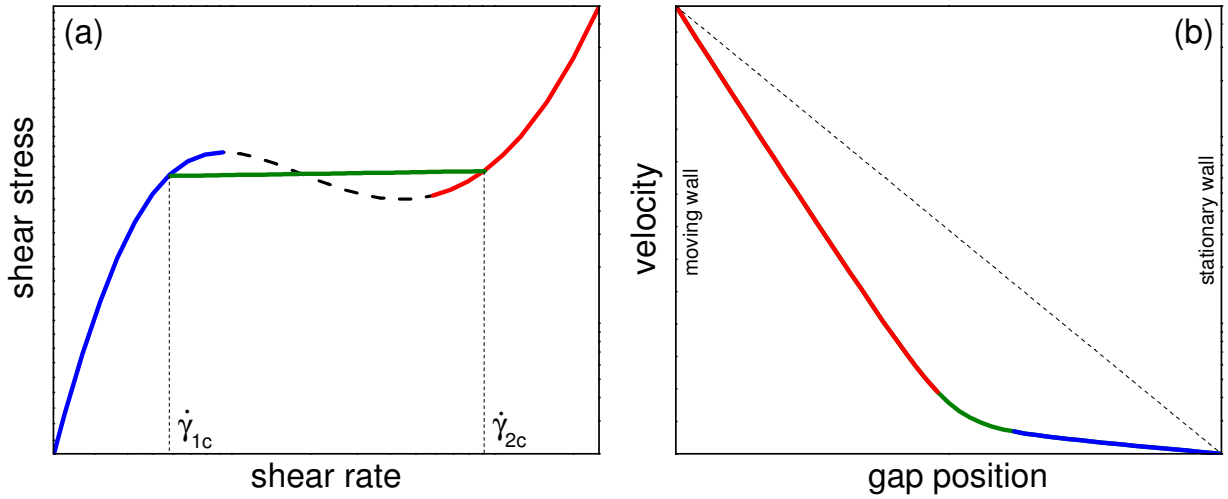

Figure 5. (a) Characteristic rheological behavior for a shear banding fluid, and (b) resulting shear banded velocity profile in Couette flow. Due to the non-monotonic behavior of the constitutive curve, the flow field separates into to stable branches of low (blue) and high (red) local shear rate with respect to the applied shear rate. The resulting coexistence between the low-shear and high-shear bands leads to a plateau in the stress (green).

Since these initial experiments, shear banding has been observed in a wide variety of different materials, including highly entangled polymers, associative polymer networks, and both hard and soft colloidal suspensions. However, wormlike micelles remain the predominant system for experimental studies of shear banding fluids. Although shear banding has come to be strictly defined in terms of inhomogeneity of the local shear rate of a material in shear flow, it has been associated with or implicated in a number of other rheological phenomena exhibited by complex fluids, including wall slip [9], yielding [10], and shear-induced phase separation (SIPS) [11,12].

Theoretical attempts to describe and predict shear banding have evolved in parallel with experiment. Despite the great variety of fluids exhibiting shear banding, and unique behaviors associated with them, many of the rheological signatures of shear banding can be captured, at least qualitatively, by non-monotonic rheological constitutive relations (Figure 5a). Shear banding is simple to conceptualize using such models, as it can be seen as the rheological equivalent of thermodynamic phase separation, where the high-shear and low-shear bands correspond to two distinct rheological states of the material. The so-called "stress plateau", then, is analogous to a thermodynamic equilibrium relation or "tie line" between the low-shear and high-shear states.

Although much work has been done to date in characterizing the rheology and flow-kinematics of shear banding wormlike micelles, little progress has been made in understanding what happens in the fluid microstructure in order to cause banding, or even what the microstructure is in the banded state. As a result, there is a broad array of proposed physical mechanisms by which shear banding occurs in specific experimental systems that is largely unconfirmed by experiment.

Recent advances in the ability to measure fluid microstructure under flow have enabled revisiting these unsolved issues in shear banding of complex fluids. The most important of these has been the development of spatially-resolved flow-SANS measurements in the flow-gradient plane of shear, which allows for the measurement of fluid microstructure at multiple locations within the flow field with microscopic precision. Because of this unique ability, researchers are beginning to address a number of important questions. What is the state of self-assembly and resulting structure in the high-shear and low-shear bands? Is the structure homogeneous within each band, and is there a sharp structural interface between bands? If banding occurs from a shear-induced phase transition as proposed, is the transition first or second order? Answers to these questions would provide more rigorous support for the proposed mechanisms of shear banding, as well as a more comprehensive understanding of the relationship between fluid microstructure and rheological properties in complex fluids.

1.3. OBJECTIVES

Shear banding fluids represent an excellent case study in the emerging complement of techniques for SANS under flow (flow-SANS). In this study, we will attempt to measure the microstructure of a model wormlike micellar system during shear banding, both as a function of the applied shear conditions and at different locations within the flow field. Along the way, we will introduce the standard compliment of techniques available for flow-SANS at the NCNR, and use

the results to demonstrate contemporary methods of data analysis for wormlike micelles and anisotropic scattering.

The model system for these measurements will be concentrated aqueous solutions of the cationic surfactant cetyltrimethylammonium bromide in the absence of added salt, where electrostatic interactions are unscreened and lead to long-range repulsions between micelles. The equilibrium phase behavior of CTAB/D_2O the concentrated regime is shown in Figure 6. At low concentrations and high temperatures, the fluid is isotropic at rest and viscoelastic, indicating the presence of wormlike micelles in solution. After a sufficient increase in concentration to ~18%, an equilibrium isotropic-nematic (I-N) transition occurs due to the packing of micelles with strong repulsive interactions.

It has long been established that CTAB solutions sufficiently close to, but not within, the equilibrium I-N phase separation binodal (grey region) can exhibit shear banding. It has been hypothesized that shear banding in this region occurs due to a shear-induced I-N transition that is essentially an extension of the equilibrium I-N transition due to flow. However, experimental evidence in early studies to prove this hypothesis was lacking. Furthermore, a critical microstructural signature differentiating shear banding and non-shear banding fluids was not identified. These shortcomings were primarily due to an inability to measure the microstructure in both the high-shear and low-shear bands.

These experiments will use flow-SANS measurements to investigate the microstructure of shear banding CTAB micelles near the I-N transition both as a function of the applied shear conditions as well as the position within the flow field. In doing so, we hope to achieve a number of experimental objectives.

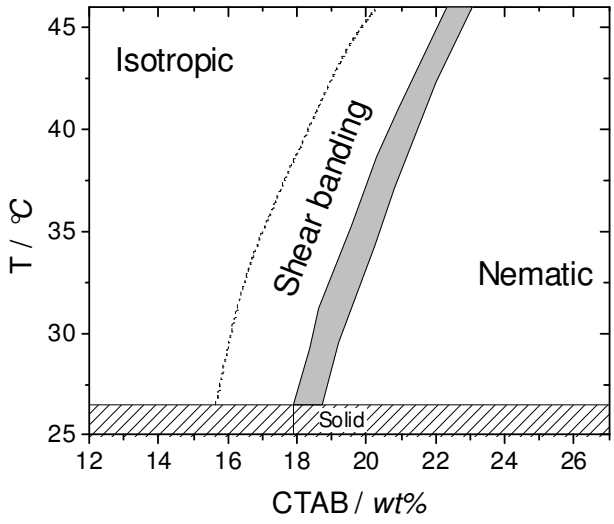

Figure 6. Equilibrium phase diagram for CTAB in D_2O near the equilibrium isotropic-nematic phase boundary (grey). Also shown is the non-equilibrium phase boundary for shear banding defined from rheological measurements.

Determine, if possible, the micellar radius, length, and charge density at equilibrium. This will be accomplished by fitting an appropriate scattering model to the data at zero shear rate.

Determine whether the structure of individual micelles, as well as the interactions between micelles, is affected by shear. This will be accomplished by analyzing the Q-dependent scattering using both circular and sector averaging.

Characterize the orientational distribution of micelles in all three scattering planes, and determine which shear plane is most useful for studying WLMs under shear. This information can be extracted by calculating moments of the annular-averaged scattering profile.

Examine the dependence of the micellar orientation and alignment on both the shear rate and the position within the flow field. Parameterizing the orientational distribution will allow for quick and efficient construction of a scattering "map" that shows how the microstructure evolves with the applied shear conditions.

Identify and contrast the microstructural state of the high-shear and low-shear bands. This will be achieved by examining both the Q-dependent scattering as well as the orientation and alignment at different conditions.

Formulate a microstructural mechanism to explain why shear banding occurs for some compositions and not others. With the previous information in hand, a clear microstructural interpretation of shear banding can be inferred.

Determine, if possible, whether the microstructural transition that occurs during shear banding is first or second order. This will be accomplished by constructing a master curve that correlates the local orientational order of the fluid and the local flow conditions.

2. EXPERIMENTAL DESIGN

Successful neutron scattering experiments require a great deal of planning beyond simply how to analyze and interpret the data. Because of the complexity and time constraints involved with obtaining and using beam time at the NCNR, one must be sure to design experiments that will maximize the chances for success. This is especially true for flow-SANS measurements, which often require a significant portion of the beam time to set up before a sample is even placed in the beam.

2.1. Why SANS?

The flow geometries used in rheometric flows (such as the Taylor Couette flows used in this experiment) require devices that can handle a wide range of torques and rotational speeds while in contact with fluids that have potentially very high viscosities, and in some cases abrasive characteristics. As such, the flow geometries are typically made from metallic materials of construction, such as aluminum and titanium (although in rare cases they can be made of quartz). This immediately prohibits the use of photon-based scattering method such as small angle light

scattering and small angle x-ray scattering. Even in cases where special transparent flow geometries can be made, the types of fluids that exhibiting interesting microstructural transitions under shear are often opaque or exhibit significant multiple scattering when using photon radiation sources. However, all of these materials are transparent to neutrons, such that existing flow devices can be easily adapted to be placed in a neutron beam, enabling SANS measurements under flow.

2.2. Scattering contrast

It is important to select the material and experimental conditions in order to make the most effective use of the beam time provided. In general, the time required for the experiments will be primarily determined by the amount of scattering from each sample, as a certain amount of scattering must be collected in order to ensure statistical accuracy of the data. As such, **it is desirable to maximize the rate at which a sample scatters neutrons** (provided, of course, that doing so does not compromise the material or the experimental objectives). This is especially important for flow-SANS measurements, as they typically require significant reduction in the size of the incident collimated neutron beam.

The **scattering intensity** is primarily influenced by two factors: the **neutron contrast** and the **concentration** (or density) of the sample. The neutron contrast, $\Delta\rho$, between a scattering object and the surrounding medium or solvent is given by

$$\Delta\rho = \rho_p - \rho_s$$

where ρ_p and ρ_s are the **scattering length density** (SLD) of the object and the solvent, respectively. The SLD for a component *i* is given by

$$\rho_i = \frac{\sum_{\{j\}} b_j}{V_i}$$

where V_i is the specific volume of component *i*, and the bound coherent scattering length for an atom or molecule *j*, b_j, is summed over all atomic or molecular components comprising component *i*.

The present experiments involve micelles of the cationic surfactant CTAB in aqueous solution. The SLD of the two phases (micelle and solvent) can be estimated assuming that the surfactant resides completely within the micellar phase, and that the water lies completely within the solvent phase[a] using the SLD calculator provided on the NCNR website. The SLD of CTAB and water, as well as their deuterated counterparts, are listed in Table 1.

Table 1. Properties of the hydrogenated compounds and their deuterated counterparts

[a] Careful surfactant scientists will recognize that this assumption is not strictly true, as (1) the micelles will always be at equilibrium with a finite concentration of surfactant monomers in the solvent phase, and (2) the solvent can partially penetrate the outer palisade layer of the micelles.

Compound	Chemical Formula	Mass density (g/cm^3)	SLD ($Å^{-2} \times 10^6$)
CTAB	$C_{19}H_{42}NBr$	0.989	-0.24
d-CTAB	$C_{19}D_{42}NBr$	1.128 (estimated)	7.06
H_2O	H_2O	0.997	-0.56
D_2O	D_2O	1.107	6.37

Table 1 suggests that the greatest neutron contrast is obtained from solutions containing deuterated surfactant and hydrogenated solvent, or vice versa. However, since D_2O is by far the more inexpensive of the two deuterated compounds, we will choose to prepare our samples using hydrogenated CTAB in D_2O. The use of D_2O is also advantageous due to its decreased incoherent scattering compared to H_2O. However, it should be noted that the thermodynamic properties and phase behavior of many compounds (especially surfactants) is sensitive to the presence of deuteration in the solvent. For example, the location of the I-N phase transition for CTAB shown in Figure 6 depends non-trivially on whether the surfactant is dissolved in H_2O, D_2O, or a combination thereof.

2.3. Sample selection and preparation

It is also important to select the samples for measurement that will best exemplify the behavior to be observed or the hypotheses to be tested. In this case, we would like to elucidate the microstructure of CTAB micelles under flow, and use this information to elucidate the microstructural transitions that underlie shear banding in the CTAB-D_2O system. Here, the sample we will choose to focus on primarily will be 16.7 wt% CTAB in D_2O at 32°C, as this is the sample for which there is the most corroborating experimental data from other measurements, including rheology, flow velocimetry and birefringence (Figure 7, right panels). We already know that this sample is shear banding, given by the non-homogeneous velocity profiles measured in the stress plateau, as well as a non-monotonic constitutive model which has been fit to the data. We also know the location of the interface between the high and low-shear bands (r*/H) for this sample, which will be valuable in designing and analyzing the flow-SANS experiments.

However, we wish to distinguish the features of the shear banding fluid that are distinct from a micellar fluid that does not exhibit shear banding. For this, we will also perform experiments on a second sample that will act as a negative control. Here, we choose 15.6 wt% CTAB in D_2O at 29°C, for which similar rheology and flow velocimetry data exist (Figure 7, left panels). Finally, because of the time constraints on the experiments, and the fact that they are typically not performed at the investigator's home institution, it is important determine how and when the samples will be prepared. The sample environments available for flow-SANS at the NCNR typically require anywhere between 5-20 mL of sample. Good preparation will involve determining the minimum sample volume required for the particular environment and flow geometry you will be using, and then bringing at least twice that amount in case a sample is compromised over the course of experiment either due to contamination, air bubbles, etc. (as is often the case in flow-SANS experiments).

When to prepare the samples is also a key consideration while designing an experiment. Many samples which show interesting behavior in flow-SANS have rheology and microstructure that depend on the sample history, and so care must be taken to ensure that the sample is handled in a controlled, reproducible manner. If a sample is to be transported from another location, the effect of conditions during transport (such as temperature variations, bumps, and vibrations) must also be taken into consideration. For example, CTAB in aqueous solution exhibits a crystallization temperature around 27°C. Therefore, if the sample is to remain a homogeneous solution, it may need to be heated during transport and storage. Because of these considerations, it may be preferable to prepare some samples at the NCNR prior to measurement.

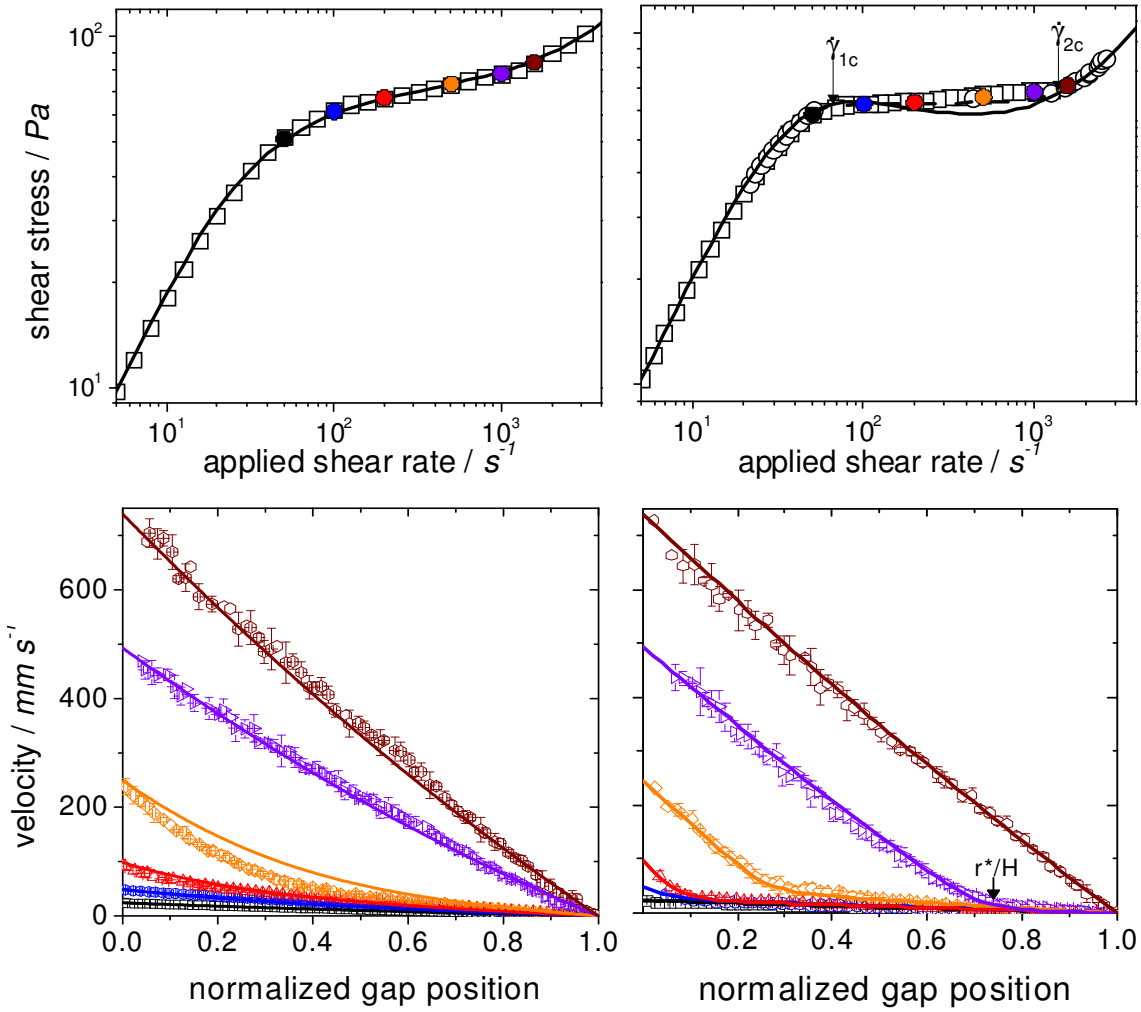

Figure 7. Comparison of steady state rheological data (top) and associated velocity profiles (bottom) for the non-shear banding (left) and shear banding (bottom) samples. The applied shear rates corresponding to curves in the bottom panels are given by the colored circles in the top panels.

2.3. Selecting a shear environment

There are several sample environments designed for SANS measurements under shear flow at the NCNR. Each of these environments is primarily composed of a **Couette concentric cylinder flow cell**. The **Rheometer** is a standard upright motor-transducer rheometer (Figure 8) that allows for simultaneous rheological and SANS measurements (**rheo-SANS**). This is advantageous for applications where offline measurement of sample rheology is difficult (e.g. for gel or paste-like samples whose rheology is highly dependent on the sample loading). The Rheometer is equipped with a Couette cell that is specially designed for neutron scattering applications. It consists of a transparent quartz outer cylinder and both quartz and titanium inner cylinders. The inner cylinder comes in several different sizes to accommodate different sample volumes and maximum shear rates/stresses. These materials of construction allow for the scattering and transmission signals measured using SANS arising from the sample environment are minimized. The temperature of the Couette cell can be controlled between -40 and 150 °C using the rheometer's native temperature control system. Because the Rheometer is… a rheometer, it is capable of performing a number of different shear protocols, including steady shear, oscillatory shear, and various shear transients, to name a few. The Rheometer can perform in both controlled shear rate mode up to 4800 s^{-1} and controlled shear stress mode up to 512 Pa. In a typical configuration, the Rheometer is placed on the Huber table, allowing for horizontal translation between the radial (1-3) and tangential (2-3) configurations (see below).

The **Boulder Shear Cell (BSC)** is an upright, motor-controlled Couette cell consisting of a moving outer cylinder and a stationary inner cylinder, both constructed of quartz (Figure 8). Both the inner and outer cylinders are available in different geometries, resulting in a number of possible gap sizes and curvatures depending on the desired sample volume and maximum shear rate. The temperature of the BSC is controlled by an external ethylene glycol bath. The strain (or strain rate) controlled motor can be operated in both steady and oscillatory shear modes. For the smaller gap configuration, shear rates of up to 3890 s^{-1} can be achieved. Although the BSC does not have the capability for online rheological measurement, it is sometimes preferable to the Rheometer, as the hardware is designed specifically to interface with the SANS data acquisition system. In a typical configuration, the BSC is placed on the Huber table, allowing for horizontal translation between the radial (1-3) and tangential (2-3) configurations (see below).

The **Porcar Shear Cell (PSC)** is a relatively new device designed for flow-SANS measurements in the 1-2 plane of shear (see below). It consists of a horizontally-mounted, short-gap Couette cell driven by a strain-controlled stepper motor (Figure 8). The motor drives an inner rotating cylinder constructed of aluminum, which is available in several radii for different gap sizes. The rotor is housed in an aluminum frame containing the outer cylinder as well as inset quartz windows through which the neutron beam is incident. The temperature of the cell is controlled by an external ethylene glycol bath. Although the motor is primarily intended for operation in steady shear mode (controlled shear rates up to 3500 s^{-1}), oscillatory shear capabilities should be available by the publication date of this report. In a typical configuration, the PSC is placed in a mounted frame, which is then placed on top of the Huber table. The mounted frame contains a small translating stepper motor that translates a beam collimating Cadmium slit across the width of the Couette cell, allowing for spatially-resolved SANS measurements across the Couette gap (see below).

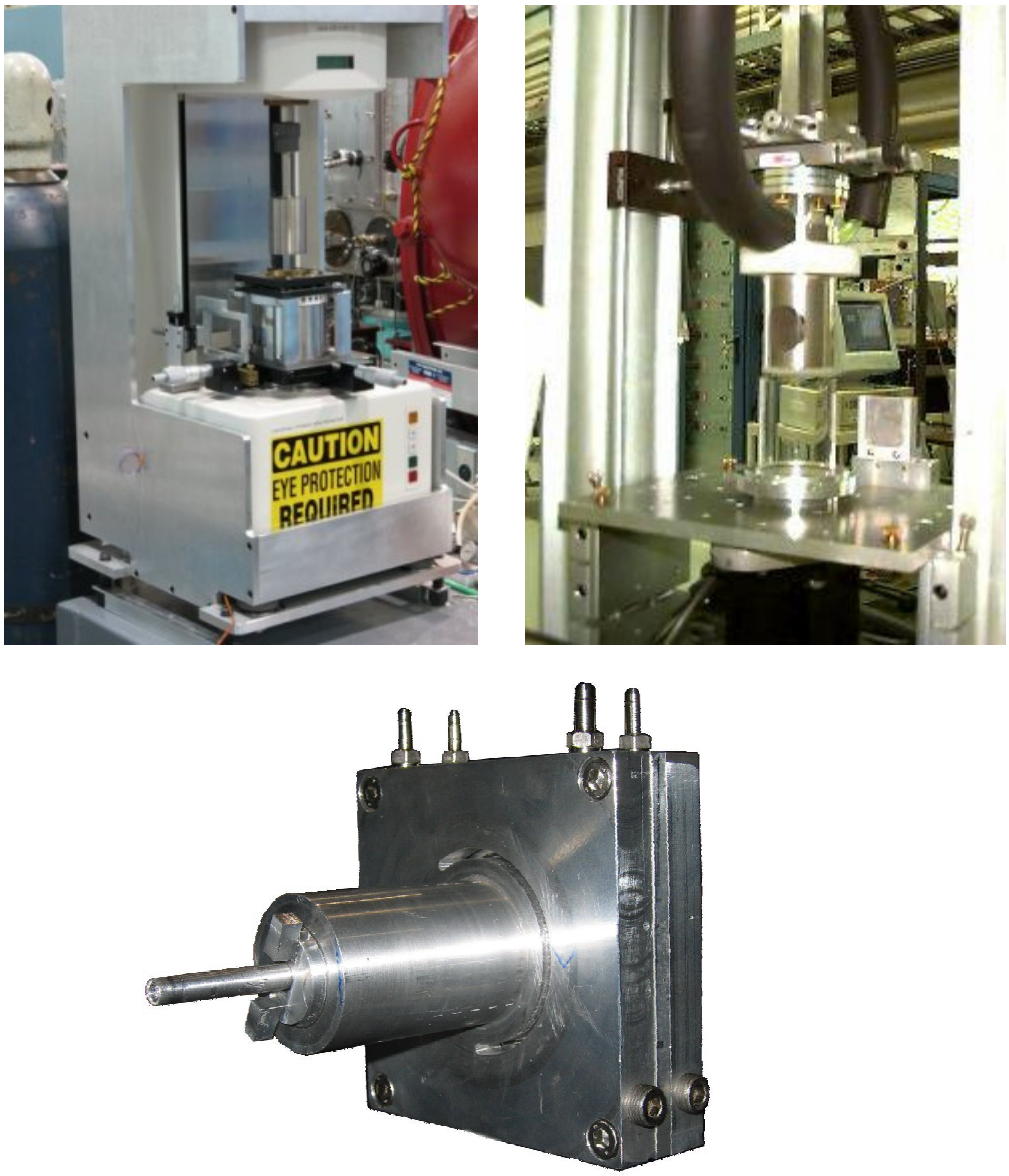

Figure 8. Photographs of the sample environments available for flow-SANS at the NCNR. Clockwise from top left: the Rheometer; the Boulder Shear Cell; the Porcar Shear Cell.

The primary difference between the upright shear cells (Rheometer and BSC) and the PSC is the scattering planes in which they permit flow-SANS measurements. In Couette geometries (as in any rheometric flow), the flow field can be decomposed into three primary directions (Figure 9). The flow direction, also known as the 1-direction (θ-direction in cylindrical coordinates), is the direction in which the velocity or force is applied (in this case, the inner or outer wall). The gradient direction, also known as the 2-direction (r-direction in cylindrical coordinates), is the direction in which the velocity must vary in order to conserve momentum. As previously mentioned, a Newtonian fluid in Couette flow will develop a linear flow-velocity profile in the

gradient direction. The final direction is the vorticity direction, also known as the 3-direction (z direction in cylindrical coordinates), is the direction orthogonal to both the flow and gradient directions. For laminar flows, the velocity in the vorticity direction is zero (or nearly zero) everywhere within the flow field, and thus it is sometimes referred to as the "neutral" direction.

Due to the directionality of the flow field, the scattering plane probed in flow-SANS will depend on the direction of the incident beam relative to these primary directions (Figure 10). This is important because many fluids develop anisotropic microstructure under flow (i.e., structure that is not, on average, spherically symmetric), and thus will produce different two-dimensional scattering patterns depending on which configuration is chosen. For example, if the shear cell is configured such that the neutron beam is parallel to the flow direction (Figure 10a), the resulting scattering plane coincides with the gradient-vorticity (2-3) plane[b] (this is often referred to as the "tangential" configuration). Therefore, the measured scattering will be a projection of the 3-dimensional fluid microstructure into the 2-3 plane. Similarly, if the neutron beam is parallel to the gradient direction (Figure 10b), the resulting scattering coincides with the flow-vorticity (1-3) plane (this is often referred to as the "radial" configuration). Finally, if the neutron beam is parallel to the vorticity direction (Figure 10c), the resulting scattering coincides with the flow-gradient (1-2) plane.

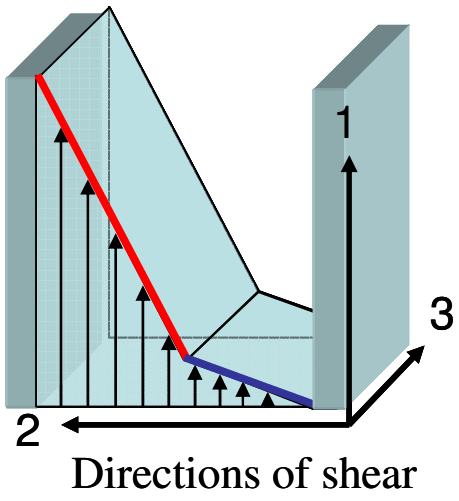

Figure 9. Illustration of the three primary directions of shear within Couette flow: (1) flow, (2) gradient, (3) vorticity. In the illustration, the left wall is moving, the right wall is stationary, and a shear banding velocity profile is depicted within the Couette gap.

[b] Note that, in reality, the Couette geometry, and thus the scattering volume, exhibits finite curvature. This produces a number of experimental artifacts in 2-3 plane flow-SANS measurements that make analysis and interpretation of the data significantly more difficult than for the other scattering planes.

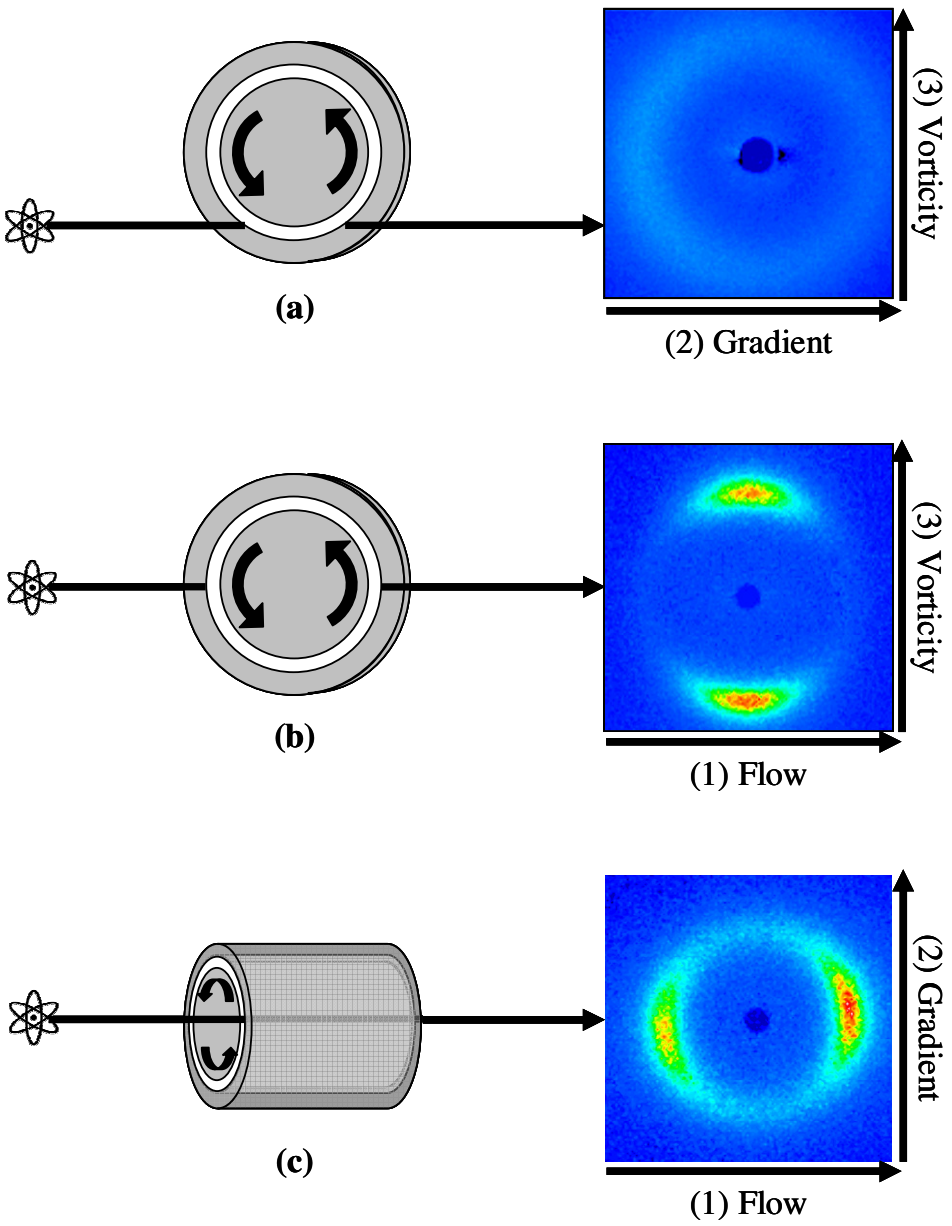

Figure 10. Beam configurations and resulting two-dimensional scattering patterns for flow-SANS measurements in the (a) gradient-vorticity (2-3) plane, (b)flow-vorticity (1-3) plane, and (c) flow-gradient (1-2) plane.

It is clear from Figure 10 that the Rheometer and the BSC can be used for flow-SANS measurements in either the flow-vorticity or gradient-vorticity planes, whereas the PSC can only be operated in the flow-gradient plane. Thus, the primary consideration in choosing between the two types of shear cells is the identification of the scattering plane that one wishes to measure the fluid microstructure in. In general, the most relevant scattering plane will depend on the particular material studied, and sometimes it is desirable to measure the scattering in all three planes of shear in order to fully characterize the anisotropic microstructure of the fluid.

In these experiments, we will use the Rheometer in the flow-vorticity plane configuration both for expedience and so that we can observe the sample rheology during measurement. However, experimental data in all three scattering planes will be provided for the data analysis section in order to demonstrate the advantages and shortcomings of each. Indeed, one of the objectives of the experiment is to identify which scattering plane is the most informative for shear banding fluids.

2.4. Selecting shear conditions

Once an appropriate shear cell environment is chosen, it is important to select the shear protocols and conditions that will be used for the flow-SANS measurement. These choices will affect not only the design of the measurement, but the analysis and interpretation of the data as well. A good experimental design for flow-SANS measurements will answer the following questions:

- Will the experiment be performed by controlling the applied shear stress or applied shear rate (or strain)?
- Will the experiment involve steady shear, oscillatory shear, or some other shear protocol?
- What particular shear rates or amplitudes will the SANS measurements be performed at? In what order will they be performed?

If the flow-SANS experiments are meant to elucidate the microstructural basis for an observed rheological behavior, the answers to these questions are typically dictated by previous experimental knowledge of that behavior. If the flow-SANS measurements are meant to investigate the response of a particular microstructure to shear flow, then it is often valuable to investigate a variety of different shear conditions in order to observe the full behavior of the material.

In these experiments, we will perform flow-SANS measurements under steady shear using applied shear rate conditions, as the shear banding transition occurs over a range of applied shear rates. First, it is important to measure the structure of the fluid at rest (0 s^{-1}). Although for this experiment this measurement will be done in the flow-SANS environment itself, the zero shear rate measurement is typically also performed using traditional static SANS measurements (such as using the 10CB environment) in order to assess any artifacts of the Rheometer and the PSC on the obtained sample scattering. This measurement is also important to check for consistency across the two sample environments, as the measured structure should be the same in both cases (for the PSC, the structure at zero shear should also be the same across the Couette gap, see below).

After measuring the structure at rest, measurements will be performed spanning the range of applied shear rates encompassing the stress plateau for the sample that exhibits shear banding (16.7 wt%, 32°C), including both before and after the critical shear rates $\dot{\gamma}_{1c}$ and $\dot{\gamma}_{2c}$ for shear banding. These shear rates are marked with colored symbols in Figure 7. We have fortuitously chosen the sample that will serve as our negative control (15.6 wt%, 29°C) such that these same shear rates fall at roughly the same relative points along the flow curve, including before, during,

and after shear thinning. This will allow us to easily discern the affects of shear banding on the fluid microstructure as distinct from those observed in shear thinning.

The experiments will be performed in order of increasing applied shear rate, beginning at 0 s^{-1}. We choose to do this because a number of problems can occur at high applied shear rates, including sample cavitation, generation of air bubbles, etc. that may compromise the sample. Furthermore, because of these potential issues, it will be important to perform a duplicate measurement (typically at 0 s^{-1}) after the entire series of shear rates in order to ensure that the sample remains intact[c].

2.5. Required q-range

In order to choose the instrument configuration, we will simulate what the expected sample scattering will look like for the samples at rest. At the chosen sample concentrations, we expect CTAB to form charged, rod-like micelles with roughly circular cross-section. Thus, we will use a model for cylindrical objects with Coulombic interactions to simulate the CTAB micelles (the "Cylinder_and_Struct.ipf" module in the SANS Analysis Igor toolbox). The volume fraction of micelles can be estimated from the concentration (here we will perform calculations for 16.7 wt% CTAB) and density (Table 1), yielding a volume fraction of ϕ=0.19. The neutron contrast between CTAB and D_2O is $\Delta\rho$ = 6.7×10^{-6} $Å^{-2}$ (Table 1). The radius of the micelles can be approximated as the length of the surfactant tail. For linear alkanes, the length of the tail l_n is given by

$$l_n = 1.54Å + 1.265n_c Å$$

where n_c is the number of carbon atoms. For CTAB (n_c = 16), this corresponds to a micellar radius of approximately r_c = 22 Å. For an estimate of the micellar length, we will assume that the micelles are approximately as long as the persistence length typically measured for CTAB wormlike micelles, L~200 Å (the micelles can be longer than this, but they will rarely be shorter.

For the Coulombic interaction model, we must specify or estimate the dielectric properties of the medium. For water at 32°C (305 K), the dielectric constant of water is approximately 78. The monovalent salt concentration for an ionic surfactant in solution is given by $c_{\pm} = \alpha_0 c_s$, where α_0 is the degree of ionization of the surfactant (~0.18 for CTAB) and c_s is the total concentration of surfactant. For 16.7 wt% CTAB (0.49 M), we obtain $c_{\pm} = 0.088$ M. We must also specify the charge on an individual micelle, given by $Q = \alpha_0 n_{agg} \approx \pi\alpha_0 r_c^2 L / V_s$, where n_{agg} is the aggregation number and V_s is the volume of a surfactant molecule, roughly given by

$$V_n = 27.4Å^3 + 26.9n_c Å^3$$

[c] Note that some samples, including non-ergodic fluids such as gels, glasses, and pastes will not retain the same equilibrium microstructure at rest after shearing, regardless of whether the sample has been contaminated or compromised. This must be taken into account when designing the flow-SANS experiment.

for linear alkanes. Substituting the known values for CTAB yields Q~150. The only remaining model parameter is the incoherent background, which for D_2O is typically ~0.06 cm^{-1}.

A plot of the simulated q-dependent scattering is shown in Figure 11. From the figure, we see that an appropriate q-range to measure the structure of the micelles will be from q_{min}~0.007 to q_{max}~0.4. This will help us to select detector settings for the instrument configuration. Specifically, we would like to determine the approximate q-range at which we expect to see significant effects of shear. For rod-like structures such as WLMs, we would expect to see some degree of alignment of the micelles. This alignment will appear strongest for the q-range over which scattering from the rod-like character of the structure is observed. In this case, this will correspond to length scales less than the micellar length, but greater than the micellar radius. Thus, one might expect that the strongest anisotropy in the scattering will be near the interaction peak at q~0.05 $Å^{-1}$ (which in this case corresponds to the length scale of nearest neighbor electrostatic interactions). Thus, we will choose one of our detector configurations such that q=0.05 A^{-1} is roughly in the center of the available q-range.

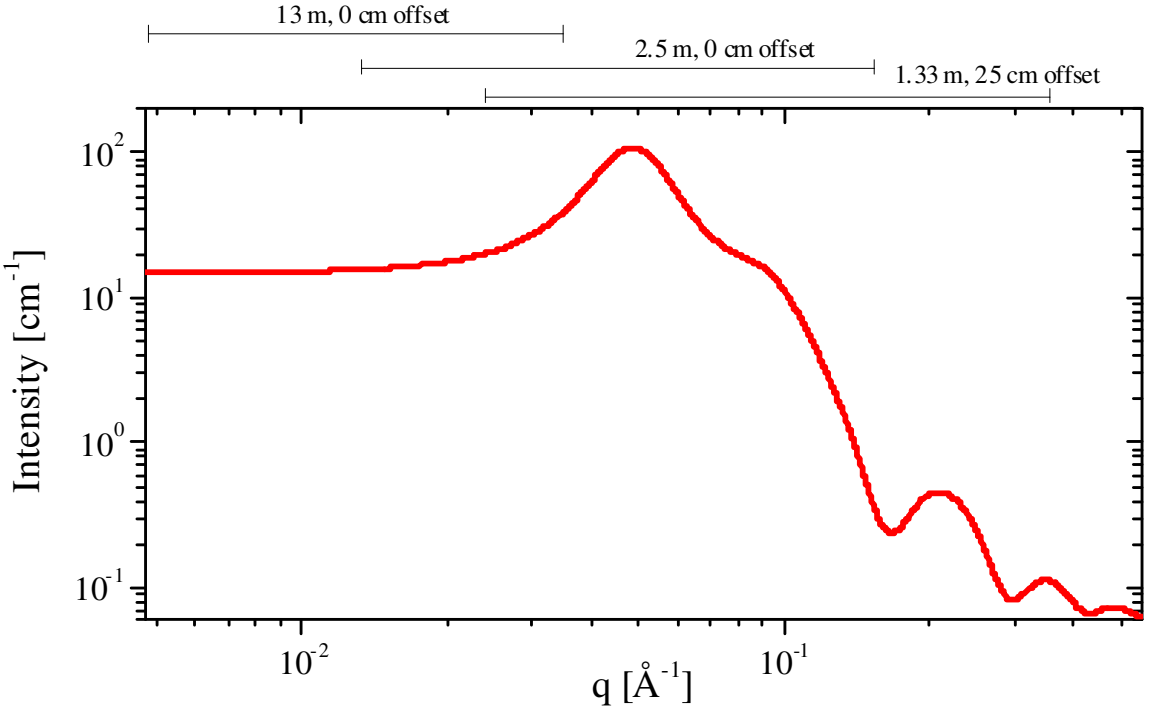

Figure 11. Simulated one-dimensional scattering profile for rigid cylinders with screened Coulombic interactions using the model parameters discussed in the text. The scales above the graph indicate the q-ranges achieved using the instrument configurations discussed in section 3.1.

3. DATA COLLECTION

3.1. Configuring the SANS instrument

A schematic of the 30-m SANS instrument is shown in Figure 12, and the instrument configuration parameters, and their allowed range for the NG3, are listed in Table 2. In order to determine the instrument configurations we wish to use for the flow-SANS experiments, we will make use of the SASCALC tool available through the NCNR.

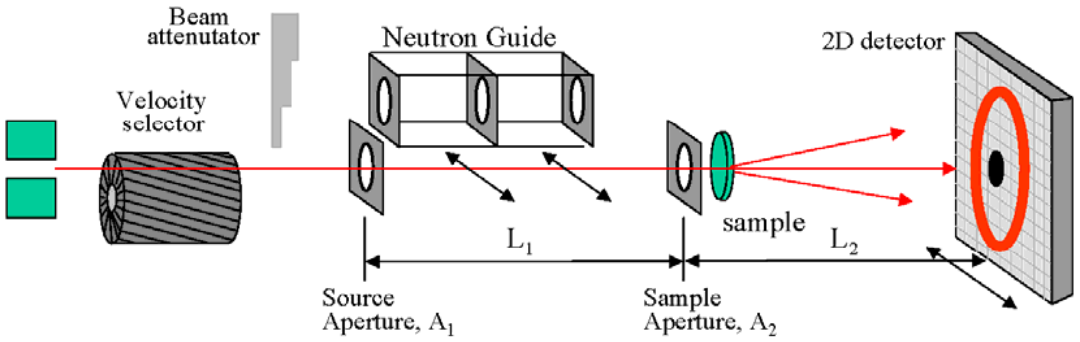

Figure 12. Schematic diagram of the components of the NCNR's 30-m SANS instruments.

Table 3. Instrument configuration parameters and their range of allowed values for the NG3 30-m SANS instrument.

Variable	**Allowed values**
Neutron wavelength	6-20 Å (determined by rotational speed of the velocity selector)
Wavelength spread (FWHM)	0.09, 0.11, or 0.22 (determined by inclination of the velocity selector)
Number of neutron guides	0-8 (determines the beam collimation by changing the distance of the source aperture from the sample)
Source aperture diameter	1.43, 2.20, or 3.81 cm for 0; 5.08 cm for 1-8 guides
Sample-to-detector distance	100-1530 cm
Detector offset	0-25 cm (detector translation perpendicular to beam to extend the Q-range covered at a given distance)
Sample aperture diameter	0-2.5cm
Beamstop diameter	2.54, 5.08, 7.62, or 10.16 cm
Beam attenuator	10 choices of beam attenuator thickness to reduce beam intensity for sample transmission measurements

There are several considerations that must be taken into account when determining instrument configurations for flow-SANS measurement. Since both the Rheometer and the PSC will be placed on the Huber table, the actual sample-to-detector distance will be greater than that anticipated by the instrument configuration software. This additional distance is 55 cm for both the Rheometer and the PSC, which is automatically added to the sample-to-detector distance input to SASCALC in order to obtain the true q-range.

For a given set of allowed parameters, SASCALC computes the corresponding q-range and the beam intensity (n/sec) on the sample. The q-range for a particular configuration is determined by the choice of wavelength, detector distance and detector offset. A wavelength of 6Å is customary for most SANS measurements, as it provides a large incident neutron flux, thus minimizing measurement time (longer wavelengths are typically used when very low q-values are desired). Similarly, a wavelength spread of $\Delta\lambda/\lambda$ of 0.12 provides an adequate balance of flux and q-resolution. In general, we choose the largest number of neutron guides (allowed in the desired q-range) in order to maximize the beam intensity on the sample. The source aperture and beam stop diameters will depend on the detector distance chose.

All that remains is to select a combination of sample-to-detector distances and detector offsets that will yield the appropriate q-range for our measurements. For the high-q limit of the instrument, we will use the shortest sample-to detector distance, 133 cm, and the maximum detector offset, 25 cm. We will choose 7 guides instead of the maximum 8 at this distance to avoid an excessive count rate on the detector, since our samples will be strongly scattering. The results from SASCALC for these choices are as follows:

```
Source Aperture Diameter = 5.00 cm
Source to Sample = 542 cm
Sample Aperture to Detector = 138 cm
Beam diameter = 3.01 cm
Beamstop diameter = 2.00 inches
Minimum Q-value = 0.0239 1/Å (sigQ/Q = 19.1 %)
Maximum Horizontal Q-value = 0.4211 1/Å
Maximum Vertical Q-value = 0.2467 1/Å
Maximum Q-value = 0.4742 1/Å (sigQ/Q = 6.2 %)
Beam Intensity = 5038230 counts/s
Figure of Merit = 1.81e+08 Å^2/s
Attenuator transmission = 0.000286 = Atten # 8
****************** NG 3 ******************
Sample Aperture Diameter = 1.27 cm
Number of Guides = 7
Sample Chamber to Detector = 133.0 cm
Sample Position is Huber
Detector Offset = 25.0 cm
Neutron Wavelength = 6.00 Å
Wavelength Spread, FWHM = 0.150
Sample Aperture to Sample Position = 5.00 cm
```

The high-q range achieved by these settings is shown in Figure 11. For the low-q limit of the instrument, we will use the longest sample-to detector distance, 1300 cm, with no detector offset. We will choose 1 guide in order to balance the achieved q-range the count rate on the detector. The results from SASCALC for these choices are as follows:

```
Source Aperture Diameter = 5.00 cm
Source to Sample = 1472 cm
Sample Aperture to Detector = 1305 cm
Beam diameter = 7.17 cm
Beamstop diameter = 3.00 inches
Minimum Q-value = 0.0035 1/Å (sigQ/Q = 30.3 %)
```

```
Maximum Horizontal Q-value = 0.0419 1/Å
Maximum Vertical Q-value = 0.0258 1/Å
Maximum Q-value = 0.0491 1/Å (sigQ/Q = 6.5 %)
Beam Intensity = 929371 counts/s
Figure of Merit = 3.35e+07 Å^2/s
Attenuator transmission = 0.00602 = Atten # 6
***************** NG 3 *****************
Sample Aperture Diameter = 1.27 cm
Number of Guides = 1
Sample Chamber to Detector = 1300.0 cm
Sample Position is Huber
Detector Offset = 20.0 cm
Neutron Wavelength = 6.00 Å
Wavelength Spread, FWHM = 0.150
Sample Aperture to Sample Position = 5.00 cm
```

The low-q range achieved by these settings is shown in Figure 11. For intermediate q-values, we wish to choose a detector distance such that the q-range will be centered around the peak in the simulated scattering data (Figure 11). After experimenting with a few values of the detector distance in SASCALC, we find that a detector distance of 250 cm with no offset will achieve our objective. As for the longest detector distance, we will choose 7 guides. The results from SASCALC for these choices are as follows:

```
Source Aperture Diameter = 5.00 cm
Source to Sample = 487 cm
Sample Aperture to Detector = 193 cm
Beam diameter = 3.94 cm
Beamstop diameter = 2.00 inches
Minimum Q-value = 0.0200 1/Å (sigQ/Q = 20.0 %)
Maximum Horizontal Q-value = 0.1765 1/Å
Maximum Vertical Q-value = 0.1765 1/Å
Maximum Q-value = 0.2470 1/Å (sigQ/Q = 5.3 %)
Beam Intensity = 4218476 counts/s
Figure of Merit = 1.52e+08 Å^2/s
Attenuator transmission = 0.000469 = Atten # 8
***************** NG 3 *****************
Sample Aperture Diameter = 1.27 cm
Number of Guides = 7
Sample Chamber to Detector = 133.0 cm
Sample Position is Huber
Detector Offset = 0.0 cm
Neutron Wavelength = 6.00 Å
Wavelength Spread, FWHM = 0.125
Sample Aperture to Sample Position = 5.00 cm
```

The low-q range achieved by these settings is shown in Figure 11. Note that this q-range also provides an adequate amount of overlap between the low-q and high-q ranges. This will be advantageous when reducing the data (see below).

It is important to mention that the beam collimation for flow-SANS measurements is different than that for most other sample environments, as the beam must be confined to a small portion of the flow geometry. These additional beam collimations will affect the total count rate.

3.2. Configuring the shear environments

Both of the shear environments require additional configuration and considerations while setting up the experiment. These primarily include collimation of the beam to the appropriate size, and alignment of the beam relative to the flow field within the flow environment.

For the Rheometer, the beam is first collimated to an 18 mm × 30 mm area using a rectangular sample beam aperture on the snout prior to the Rheometer. For 1-3 plane measurements (Figure 10b), the beam is further reduced using an additional 12 mm x 18 mm aperture affixed to the central diameter of the Couette cell. Alignment of the 1-3 plane is then accomplished by adjusting the tilt and translation of the rheometer alignment axis with respect to the sample aperture. For 2-3 plane measurements (Figure 10a), the beam is further reduced using an 0.4 mm x 18 mm slit affixed along the tangent of the Couette cell. Alignment of the 2-3 plane is then accomplished by performing a transmission scan under translation of the Huber table, similar to the method by which the gap is calibrated in the PSC (see below).

For the PSC, the beam is first collimated to an 4 mm x 20 mm area using a rectangular sample beam aperture on the snout prior to the shear cell. For 1-2 plane measurements (Figure 10c), the beam is further reduced using a 5 mm high slit affixed to the face of the shear cell closest to the beam snout. This slit is oriented horizontally along the radial direction of the shear cell, such that the beam is confined to the area in which the flow is in the vertical direction. A final 3 mm high slit is mounted on the arm of the stepper motor housed on the PSC frame. The width of this slit can be chosen to be 0.13, 0.25, 0.5, or 1.0 mm, depending on the desired spatial resolution within the Couette gap[d].

Alignment of the 1-2 plane scattering in the PSC is typically done via a two-step process. In the first step, the stepper motor position is coarsely adjusted so that the vertical slit is moved completely out of the beam path. Then, the translation of the Huber table is adjusted so that the laser mounted along the path of the direct beam (visible when the beam is off) is visible through the horizontal slit and the two quartz windows on the shear cell, indicating that the direct beam is aligned along the 1-2 plane of the shear cell. In the second step, the vertical slit is moved back into the beam path, such that it is approximately just to one side of the Couette gap. The exact location of the gap is then calibrated by performing a series of transmission measurements (see below) in which the stepper motor is used to move the vertical slit across the Couette gap in small increments. For best results, this calibration should be done with the sample loaded within the shear cell in order to maximize the contrast with respect to the aluminum shear cell.

[d] There is a tradeoff to be considered when selecting a vertical slit width. On one hand, smaller slit sizes mean that the scattering signal is averaged (smeared) over a smaller area, resulting in better spatial resolution of the structure. On the other hand, larger slit widths will result in a higher incident neutron flux.

The results of such a measurement are shown in Figure 13, which plots the measured transmission counts as a function of the slit motor position for a 1.35 mm gap rotor and 16.7 wt% CTAB loaded in the shear cell, with a 0.1 mm vertical slit. At a motor position of -4°, the collimated beam passes through the area to the left of the Couette gap, which consists primarily of aluminum. As the vertical slit is scanned to the right, it proceeds through the aluminum until it eventually begins to contain the inner wall of the Couette gap. At this point, the transmission decreases as the fraction of the slit occupied by the gap increases (due to the lower transmission of the sample relative to aluminum). Eventually, the entire slit will be located within the volume of the gap, and the transmission will reach a roughly constant value. This will proceed as long as the vertical slit is entirely within the Couette gap. Finally, the slit will begin to contain portions of the aluminum housing on the outer wall of the gap, at which point the transmission will begin to increase as the slit is scanned further. Using this transmission scan, the Couette gap is then defined by the region over which the sample transmission is constant (in this case, from -2° to 2.5°). The actual distance this range of motor positions corresponds to is equal to the gap corresponding to the inner rotor used (1.35 mm in this case).

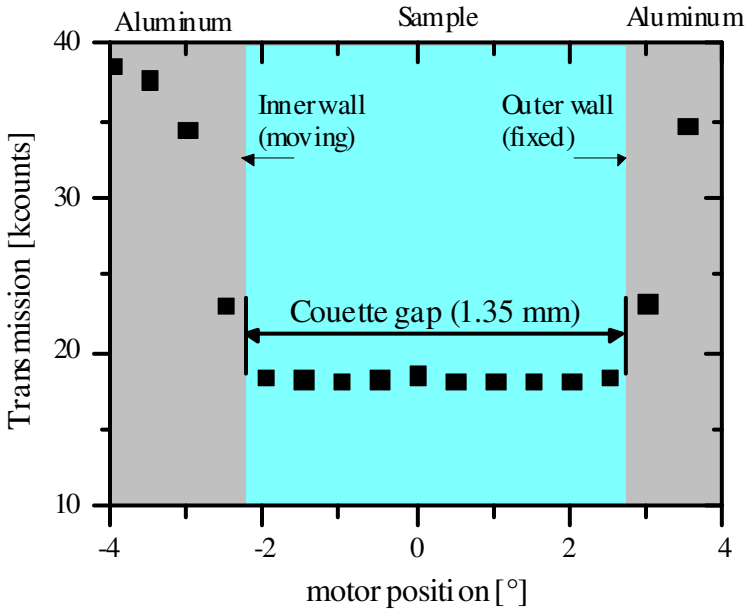

Figure 13. Transmission measured at several vertical slit motor positions used in locating the Couette gap in the Porcar Shear Cell for spatially-resolved 1-2 plane flow-SANS measurements. The resulting motor calibration for the geometry gap is indicated.

Once the gap is calibrated, we must choose the slit positions at which we will measure the sample scattering under shear for the chosen applied shear rates. Because we anticipate the structure of the fluid to depend strongly on the gap position (at least for the shear banding sample), we will choose 7 different slit positions beginning at -1.5° and increasing to 2.1° in increments of 0.6°. We choose these lower and upper limits on the motor position so that we

avoid collecting scattering very close to the edges of the gap, as significant artifacts are obtained when the beam is of grazing incidence with respect to the aluminum walls.

3.3. What measurements to make

In general, counts recorded by the detector with the sample in place can come from 3 sources: 1) neutrons scattered by the sample itself (the scattering we are interested in); 2) neutrons scattering from something other than the sample, but which pass through the sample; and 3) everything else, including neutrons that reach the detector without passing through the sample (stray neutrons or so-called room background) and electronic noise in the detector itself. To separate these three contributions, we need three measurements:

i) Scattering measured with the sample in place (which contains contribution from all 3 sources listed above), denoted $\boldsymbol{I_{sam}}$. This measurement will be made for each sample, shear rate, and gap position (for the PSC) we are interested in.
ii) Scattering measured with the empty Rheometer or BSC in place (which contains contributions from the 2nd and 3rd sources listed above), denoted $\boldsymbol{I_{emp}}$. This measurement will be made at only one shear rate (0 s^{-1}), but at all gap positions (for the PSC).
iii) Counts measured with a complete absorber ("blocked beam") at the sample position (which contains only the contribution from the 3rd source listed above), denoted $\boldsymbol{I_{bgd}}$. This measurement will be made only once for each flow environment with the flow cell in place (with or without sample).

In addition to these three 'scattering' measurements, the transmission (the fraction of the incident beam intensity that passes through the sample without being scattered or absorbed) of the sample and the sample cell must also be measured in order to correctly subtract the contributions to the background and to calibrate the scattering on an absolute cross section scale (see below). The transmission is measured by inserting a calibrated attenuator in the incident beam (to reduce the direct beam intensity to an accurately measurable level) and measuring the direct beam intensity with and without the sample in the respective flow environments. The ratio of these two short measurements (typically 1-2 minutes each) is the sample (or sample cell) transmission. For flow-SANS measurements, it is important to measure the sample transmission at every applied shear rate (and every gap position). This information can be used in order to determine if the sample was compromised in any way during the course of measurement.

3.4. How long to count

A SANS experiment is an example of the type of counting experiment where the uncertainty, or more precisely the standard deviation, σ, in the number of counts recorded in time, *I(t)*, is $\sigma \sim \sqrt{I(t)}$. If the scattering is roughly evenly distributed over the SANS detector, then a good rule of thumb is that one should accumulate about 500,000 total detector counts per sample

measurement[e]. For example, if the accumulated counts are circularly averaged (see below), one obtains about 50 data points when plotting *I(q)* versus *q*. This amounts to about 1000 counts per data point with a standard deviation of $\sqrt{1000} \sim 30$ or an uncertainty of about 3 %, which is good enough for most purposes.

A related question, is how long should the background and empty cell measurements be counted relative to the sample measurement. The same $\sigma \sim \sqrt{I(t)}$ relationship leads to the following approximate result for the optimal relative counting times

$$\frac{t_{background}}{t_{sample}} \sim \sqrt{\frac{Count\ Rate_{background}}{Count\ Rate_{sample}}}$$

Hence if the scattering from the sample is weak, the background should be counted for as long (but no longer!) as the sample scattering. However, if the sample scattering count rate is, say, 4 times greater than the background rate, the background should be counting only half as long as the sample scattering.

4. DATA REDUCTION

4.1. Data correction

Data reduction begins by correcting the measured scattering from the sample for the sources of background discussed previously, and multiplying the corrected counts by a scaling factor (to remove incidental differences between measurements such as the counting time and sample thickness) that puts the data on an absolute scale of scattering cross section per unit volume. The background-corrected neutron counts, $I_{cor}(q_x,q_y)$, recorded in a detector pixel in a time interval t are related to absolute cross section, $d\Sigma(q_x,q_y)/d\Omega$, through the expression

$$I_{cor}\left(q_x, q_y\right) = \phi\ A\ \Delta\Omega\ \varepsilon\ t\ d\ T\ \frac{d\Sigma\left(q_x, q_y\right)}{d\Omega}$$

where:

ϕ = the neutron flux (neutrons/cm2-sec) at the sample
A = the area of the beam incident on the sample
d = the sample thickness
T = the transmission of the sample (and its container, if there is one)
$\Delta\Omega$ = the solid angle subtended by one pixel of the detector
ε = the detector efficiency, and
t = the counting time.

[e] Note that, due to the significantly reduced beam size, a count total of 500,000 for each shear condition or gap position may not be feasible. In these cases, one should find an acceptable tradeoff between the statistical precision and the number of different conditions measured.

The incidental instrumental factors can be lumped together into one constant, $K = \phi\ A\ \Delta\Omega\ \varepsilon\ t$, and the intrinsic quantity $d\Sigma(q_x,q_y)/d\Omega$, the differential scattering cross section per unit volume, is obtained by scaling the recorded counts

$$\frac{d\Sigma\left(q_x,q_y\right)}{d\Omega} = \frac{I_{cor}\left(q_x,q_y\right)}{KdT}$$

We now go over the specific steps involved in extracting $d\Sigma(q)/d\Omega$ from the raw data. The raw scattered intensity measured from the sample, I_{sam}, and the empty cell, I_{emp}, can be written as

$$I_{sam}\left(q_x,q_y\right) = KdT_{sample+cell}\left[\left(\frac{d\Sigma\left(q_x,q_y\right)}{d\Omega}\right)_{sam} + \left(\frac{d\Sigma\left(q_x,q_y\right)}{d\Omega}\right)_{emp}\right] + I_{bgd}\left(q_x,q_y\right)$$

$$I_{emp}\left(q_x,q_y\right) = KdT_{cell}\left(\frac{d\Sigma\left(q_x,q_y\right)}{d\Omega}\right)_{emp} + I_{bgd}\left(q_x,q_y\right)$$

where $T_{sample+cell}$ and T_{cell} are the measured transmission of the sample (in its respective flow environment) and the empty flow cell, respectively. From the above, the background corrected scattering, denoted I_{cor}, is given by

$$I_{cor}\left(q_x,q_y\right) = \left[I_{sam}\left(q_x,q_y\right) - I_{bgd}\left(q_x,q_y\right)\right] - \frac{T_{sample+cell}}{T_{cell}}\left[I_{emp}\left(q_x,q_y\right) - I_{bgd}\left(q_x,q_y\right)\right]$$

The corrected counts, I_{cor}, are proportional to the quantity of interest, namely the differential scattering cross section. From the above equations,

$$I_{cor}\left(q_x,q_y\right) = KdT_{sample+cell}\frac{d\Sigma\left(q_x,q_y\right)}{d\Omega}$$

The instrumental scale factor, K, will be determined from a measurement of the attenuated direct beam intensity,

$$I_{direct} = KT_{atten}$$

where T_{atten} is the transmission of a calibrated attenuator. The result of the data correction is a two-dimensional absolute, corrected scattering intensity $I_{cor}\left(q_x,q_y\right)$ as a function of the q-values (corresponding to detector pixels) q_x and q_y.

4.2. Data averaging

Once $I_{cor}(q_x,q_y)$, several types of data averaging can performed based on the desired application of the data. Visual examples of the various reduction protocols and their resulting SANS spectra for a sample two-dimensional scattering pattern are shown in Figure 14 for a sample under shear exhibiting anisotropic scattering. Circular averaging (Figure 14a) is used to compute the average, angle-independent scattered intensity, $I(q)$. This is done by averaging $I_{cor}(q_x,q_y)$ at a given radial q-value, q, over all azimuthal angles, and repeating this procedure for all values of q. In the NCNR Data Reduction package for Igor, circular averaging is performed by selecting the "Circular" AVTYPE when building a reduction protocol. Note that this type of averaging eliminates the anisotropy from the data, which should be taken into account when analyzing the data.

Annular averaging (Figure 14b) is used to compute the angle-dependent scattering, $I(q^*,\phi)$, at a given radial q-value, q^*. This is done by constructing a centrosymmetric annulus centered at q^* with a width of Δ (in pixels). $I(q^*,\theta)$ is then computed by averaging $I_{cor}(q_x,q_y)$ on the interval $q=[q-\Delta/2,\ q+\Delta/2]$ for a particular value of θ, and then repeating the process for all values of θ. In the NCNR Data Reduction package for Igor, annular averaging is performed by selecting the "Annular" AVTYPE when building a reduction protocol, and defining the central q-value and pixel width of the annulus.

Sector averaging (Figure 14c) is used to compute the average, angle-independent scattered intensity, $I(q,\phi_{ref})$ over a given range of azimuthal angles $\Delta\theta$. This is done by averaging $I_{cor}(q_x,q_y)$ at a given radial q-value, q, over the set of azimuthal angles defined by $\Delta\theta$, and repeating this procedure for all values of q. In the NCNR Data Reduction package for Igor, circular averaging is performed by selecting the "Sector" AVTYPE when building a reduction protocol, and defining the azimuthal range $\Delta\theta$ and the central orientation angle, ϕ_{ref}. For flow-SANS data, is important to define ϕ_{ref} such that it corresponds to one of the principal directions of flow. For scattering in the 1-3 plane, $\phi_{ref} = 0^o$ corresponds to the flow direction, and $\phi_{ref} = 90^o$ corresponds to the vorticity direction. For scattering in the 2-3 plane, $\phi_{ref} = 0^o$ corresponds to the gradient direction, and $\phi_{ref} = 90^o$ corresponds to the vorticity direction. For scattering in the 1-2 plane, $\phi_{ref} = 0^o$ corresponds to the flow direction, and $\phi_{ref} = 90^o$ corresponds to the gradient direction.

5. DATA ANALYSIS

5.1. Characterizing the micellar structure

The objective of this part is to characterize the micellar structure at rest. This will be accomplished by analyzing the circularly-averaged corrected intensity, $I(q)$. Assuming that the scattering from all micelles can be modeled as the scattering from an equal number of micelles with average size and shape, and that the scattering due to the structure of an individual micelle and due to interactions between micelles can be separated, $I(q)$ can be modeled using the factorization approximation,

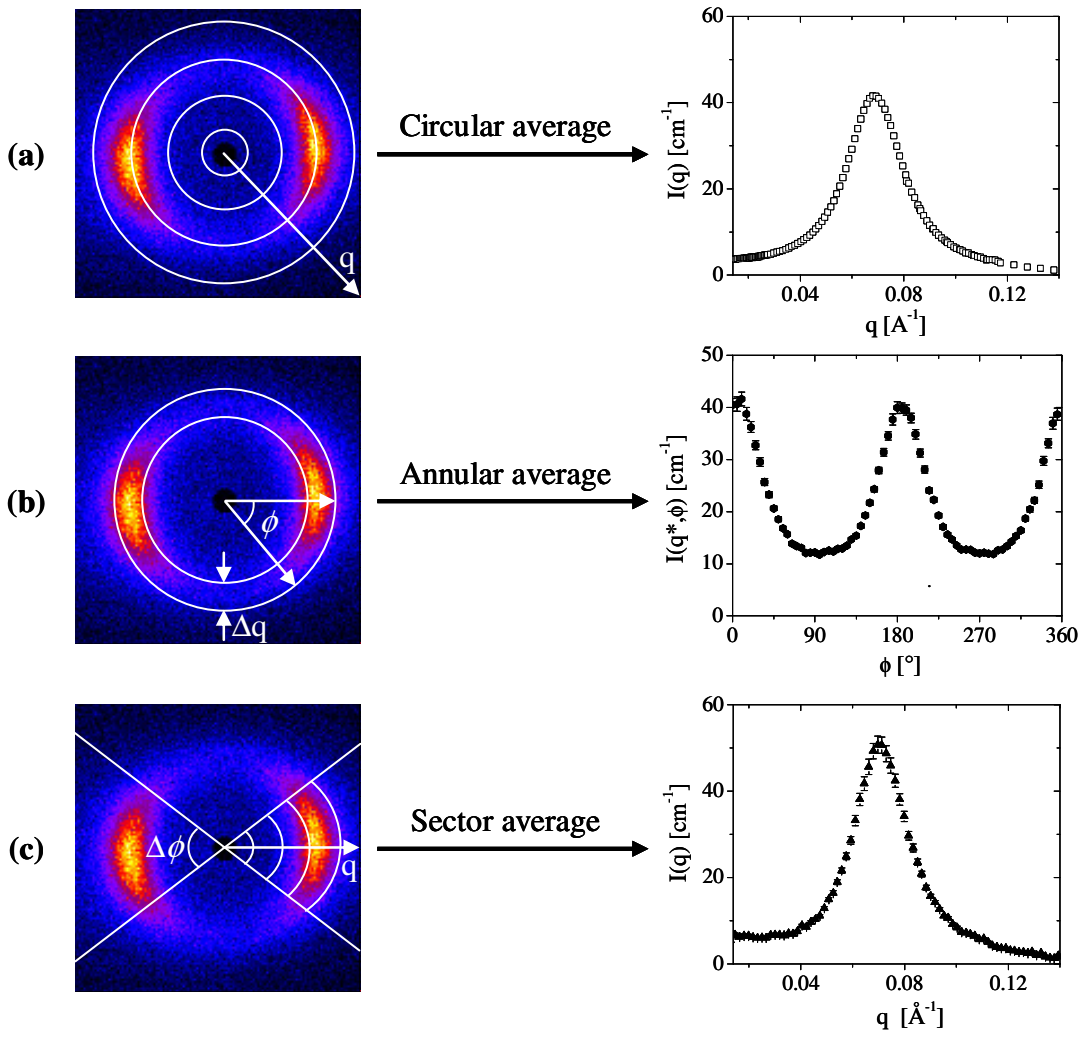

Figure 14. Schematic of SANS data reduction (left) and resulting absolute scattered intensity data (right) for (a) circular averaging, (b) annular averaging, and (c) sector averaging.

$$I(q) = (\Delta\rho)^2 V_p^2 N_p P(q) S(q) + I_{inc}$$

where V_p and N_p are the volume and number density, respectively, of micelles, $P(q)$ is the "form factor" describing scattering from the mass distribution within a micelle, $S(q)$ is the "structure factor" describing scattering from the intermicellar interactions, and I_{inc} is the incoherent scattering cross-section. The factorization approximation corresponds to separability of $P(q)$ and $S(q)$. This approximation is strictly valid only for isotropic interactions between scattering objects. For structures whose morphology is anisotropic (such as rodlike or wormlike micelles), the factorization approximation can still be used, but under a number of other assumptions to take into account the anisotropic nature of the interactions. However, the details of these theories are beyond the scope of this tutorial.

The form factor is related to the real-space micellar structure by

$$P(\mathbf{q}) = \int \left(p(\mathbf{r_{ij}}) \right)^2 \exp\left(i\mathbf{q} \cdot \mathbf{r_{ij}} \right) d\mathbf{r_{ij}}$$

where $p(\mathbf{r_{ij}})$ is the pair correlation function. The structure factor is related to the real space distribution of micelles within the sample by

$$S(q) = 1 + \int \left[g(r_{12}) - 1 \right] \exp\left(iq \cdot r_{12} \right) d^3 r_{12}$$

where $g(r_{12})$ is the radial distribution function, which can be calculated by assuming a model for the pairwise interactions between scattering objects. In the limit of $q \rightarrow 0$, the above expression for $I(q)$ is drastically simplified to

$$I(q) = I(0) \exp\left(\frac{q^2 R_g^2}{3} \right) + I_{inc}$$

where R_g is the average radius of gyration of a micelle. This relationship (known as a "Guinier analysis") is typically valid for $qR_g < 1$. For larger q-values, appropriate models must be chosen for $P(q)$ and $S(q)$ in order to fit $I(q)$ and gather structural information, including the micellar radius, length, and interactions. Here, we will explore the use of several different models, including monodisperse and polydisperse cylinders and ellipsoids for the form factor, and hard sphere, square well, and screened Coulombic intermicellar interactions. This will be done in order to answer the following questions:

- Can the radius of gyration of the micelles be resolved for these samples? The micellar length? The micellar radius?
- Can the interactions between micelles be neglected ($S(q)$=1), as in dilute systems?
- Are the interactions between micelles attractive or repulsive?
- If an interaction peak in the scattering is observed, can it be used to gain further information about the sample?

5.2. Determining the effect of shear on micellar structure

The objective of this part will be to assess changes (if any) in the micellar structure and interactions upon the application of shear. Because the structure will depend (in general) upon both the applied shear rate and the location in the gap, this will require performing analysis on a number of different conditions, including (I) shear rates prior to shear thinning, (II) shear rates during shear thinning or shear banding, and (III) shear rates after shear thinning or shear banding. For measurements in the 1-2 plane using the PSC, the analysis will also be performed for several positions within the gap to determine if the micellar structure is homogeneous across the flow field.

The analysis for this part will be done primarily by analyzing sector-averaged data in the 1-3 and 1-2 scattering planes using the same models as in the previous section. Judging from the scattering images in Figure 14, the scattering will be stronger in one direction of shear compared to the others. Thus, it is often assumed that the scattering is a superposition of two contributions, one from the scattering that is aligned along the direction of strong scattering (due to structures that are aligned in that direction), and one from scattering that is isotropic over all directions (due to structures that are randomly oriented within the fluid). Sector-averaged scattering data will be analyzed under this assumption will be used to answer the following questions:

- Is the micellar radius (or length, if determinable) significantly changed by the application of shear in regions I, II, or III?
- Does the application of shear result in changes in intermicellar interactions? If so, how?
- Which direction of shear are the micelles primarily oriented in?
- Do the aligned micelles possess different structure or interactions compared to the isotropic micelles?

5.3. Characterizing the orientational distribution

The primary difference between SANS under static conditions and SANS under flow is the presence (for most materials) of significant anisotropy in the scattering due to changes in the orientations of scattering objects. For example, consider a fluid comprised of rod-like objects (Figure 15), each having orientation ψ with respect to some reference angle, such that the overall fluid exhibits a distribution function, $f(\psi)$, describing the probability of finding a given orientation of an individual rod. For an isotropic fluid at equilibrium (at sufficiently low volume fraction of rods), there is no preferred orientation of the rods, and so $f(\psi)$ is uniform over all ψ (Figure 15, left panel). However, under shear, thermodynamic and hydrodynamic interactions conspire to orient the rods along a preferred direction[f], ψ_0, such that $f(\psi)$ will exhibit a local maximum at ψ_0 and a corresponding local minimum at $\psi_0 \pm \pi/2$ (Figure 15, right panel).

The fact that the orientational distribution of scattering objects is non-uniform under shear requires us to analyze the scattering by assuming a certain characteristic form for $f(\psi)$. For rod-like scattering objects (such as wormlike micelles), $f(\psi)$ has been theoretically described by the Maier-Saupe distribution

$$f(\psi) = \frac{1}{Z} P_2\left(\cos(\psi - \psi_0)\right)$$

where Z is a normalization constant, and $P_2(x) = \left(3x^2 - 1\right)/2$ is the second order Legendre polynomial.

[f] Note that this preferred direction need not be the flow direction, as the experimental analysis will show.

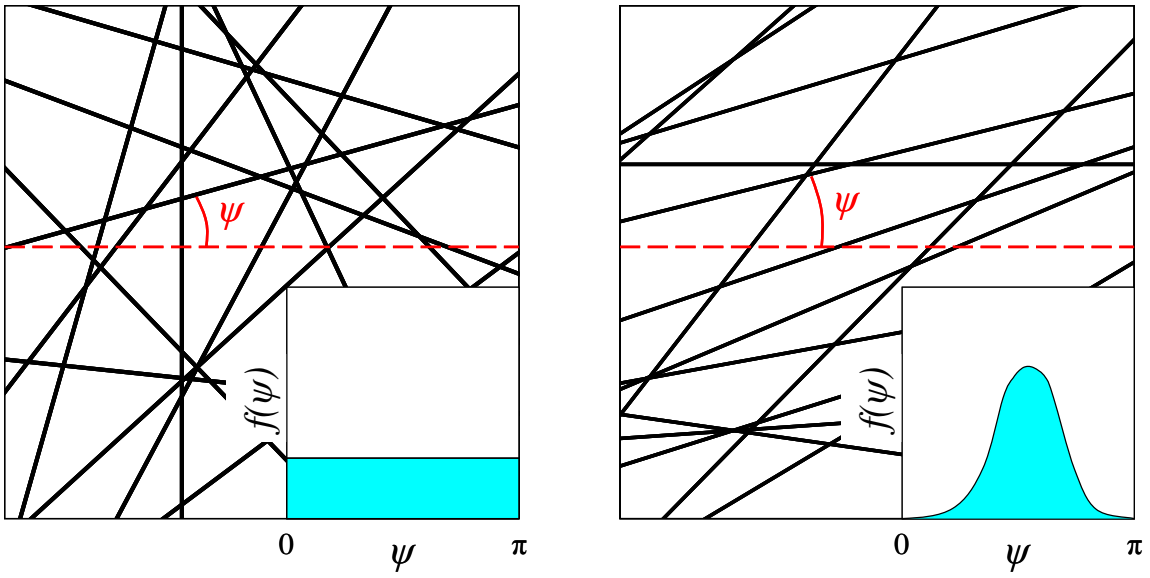

Figure 15. Illustrations and orientational probability distribution functions (inset) for a fluid of rigid rods with isotropic (left) and anisotropic orientation.

We can immediately define two characteristic moments of this orientational distribution. The first, ψ_0, is the average orientation of scattering objects, as mentioned previously. The second is the alignment factor, which describes the breadth of the orientational distribution about ψ_0, and is given by

$$a_f = \frac{\int f(\psi)\cos^2(\psi-\psi_0)\,d\psi}{\int f(\psi)\,d\psi}.$$

A value of $a_f = 0$ corresponds to a completely isotropic fluid, whereas $a_f = 1$ corresponds to a fluid which is perfectly aligned at ψ_0.

In order to apply this distribution to analysis of the SANS data, we must make several restrictive assumptions. First, since the SANS pattern is a two-dimensional projection of a three-dimensional orientational distribution, we must assume that scattering from objects oriented out of the scattering plane will be isotropic when projected into the scattering plane (i.e., there is not a preferred out-of-plane orientation). Subsequently, if we assume that the orientational contribution to the scattering is separable from the form (q-dependent) contribution, then the coherent scattering intensity can be written as

$$I(q,\phi) \approx I_{\max}(q)\,\hat{F}(\theta) + I_{inc}$$

where $I_{\max}(q)$ is an isotropic term (which contains the scattering length density, number density of scattering objects), and $\hat{F}(\theta)$ is the Fourier transform of $f(\psi)$. $\hat{F}(\theta)$ can then be empirically fit by an expression reminiscent of $f(\psi)$, namely

$$\hat{F}(\theta) = \exp\left\{\alpha\left[P_2\left(\cos\left(\theta-\theta_0\right)\right)-1\right]\right\}$$

where α is an empirical constant. Note that, due to the Fourier transform of $f(\psi)$, $\theta_0 = \psi_0 \pm \pi$. Thus, the annular averaged scattering intensity, $I(q^*,\theta)$, will be given by

$$I(q^*,\theta) = I_{\max}(q^*)\exp\left\{\alpha\left[P_2\left(\cos\left(\theta-\theta_0\right)\right)-1\right]\right\} + I_{inc}\,.$$

By fitting $I(q^*,\theta)$ to this expression, one can thus obtain ψ_0 for the fluid (given by the angle at which $I(q^*,\theta)$ exhibits a local minimum). The angle-dependent scattering intensity can be integrated similarly to the expression for a_f to obtain the scattering alignment factor in the relevant scattering plane

$$A_f(q) = -\frac{\int_0^{2\pi} I_c(q,\theta)\cos\left[2\left(\theta-\theta_0\right)\right]d\theta}{\int_0^{2\pi} I_c(q,\theta)d\theta}\,.$$

Previous work has shown that a_f and A_f are identical in the low-q limit where the approximations described above are valid and A_f is independent of q. Thus, A_f is a reasonable parameterization of the orientational distribution to compare with theory for a number of anisotropic fluids. Experimentally, A_f is calculated by numerical integration of $I(q^*,\theta)$.

From measurements of $I(q^*,\theta)$, the above analysis will be used to characterize the orientational distribution of the shear banding and non-shear banding samples as a function of applied shear rate (for 1-3 and 1-2 plane flow-SANS) and gap position (for 1-2 plane flow-SANS). This analysis will be used to answer the following questions:

- Which scattering plane provides the most information for the shear banding wormlike micelles? What information does this scattering plane provide that the others do not?
- For a given scattering pattern, how do ψ_0 and A_f depend on the q-value at which they are calculated? Is there a q-value at which these parameters become q-independent? If so, what length scale does this correspond to in terms of the micelles?
- For the shear banding sample, what orientational states do the low-shear and high-shear bands correspond to (hint: previous measurements have shown $\psi_0 \sim 0°$ and $A_f \sim 0.6$ for CTAB concentrations where the sample is a nematic phase at rest)?
- For 1-3 plane flow-SANS, how do the values of ψ_0 and A_f as a function of the applied shear rate compare between the shear banding and non-shear banding samples?

- For 1-2 plane flow-SANS, how do the profiles of ψ_0 and A_f across the gap compare between the shear banding and non-shear banding samples for applied shear rates where shear banding is observed?
- With the above information in hand, why do some fluids shear band and others don't?
- Is the transition in the orientational distribution observed during shear banding first order or second order?
- Are the values of ψ_0 and A_f measured in the 1-3 plane simply a spatial average of their values in the 1-2 plane, as has been sometimes assumed?